43rd AIAA Plasmadynamics and Lasers Conference
25 - 28 June 2012, New Orleans, Louisiana

AIAA 2012-3091

Microscale Dielectric Barrier Discharge Plasma Actuators: Performance Characterization and Numerical Comparison

Justin C. Zito[1] and David P. Arnold[2]
Interdisciplinary Microsystems Group, Dept. of Electrical and Computer Engineering, University of Florida, Gainesville, FL, 32611, USA

Tomas Houba[3], Jignesh Soni[4], Ryan J. Durscher[5] and Subrata Roy[6]
Applied Physics Research Group, Dept. of Mechanical and Aerospace Engineering, University of Florida, Gainesville, FL, 32611, USA

Dielectric barrier discharge (DBD) plasma devices have been designed and manufactured with microscale dimensions utilizing semiconductor fabrication techniques. Particle image velocimetry (PIV) measurements indicate induced wall jet velocities up to 2.0 m/s. Direct force measurements using a torsional balance indicate thrust values up to 3 mN/m at 5 kV_{pp} and 1 kHz and consume an average power of 15 W/m. The measured thrust data is applied in a numerical model to compare simulated velocity flow fields with experimental PIV data. The model shows good agreement with experimental data for the velocity and wall jet thickness for macro device geometries, but inaccurately predicts the downstream velocity decay. Microscale devices demonstrated equivalent 'thrust effectiveness' to macroscale actuators, but with a 31% improvement in mechanical-to-electrical energy conversion efficiency. The microscale DBD actuators occupy an order of magnitude reduction in device footprint and mass, and potentially enable large arrays for distributed flow control applications.

Nomenclature

δ	=	logarithmic decrement
η	=	energy conversion efficiency
ε_r	=	relative permittivity
E_d	=	dielectric strength
F	=	force
I	=	current
k_θ	=	torsional spring constant
l	=	moment arm length
N	=	number data points
P	=	power
θ	=	angle of deflection
v	=	fluid velocity
V	=	voltage

[1] Graduate Research Assistant, Electrical and Computer Engineering, 332 Benton Hall, Gainesville, FL 32611, Student Member AIAA.
[2] Associate Professor, Electrical and Computer Engineering, 229 Benton Hall, Gainesville, FL 32611, Member AIAA.
[3] Graduate Research Assistant, Mechanical and Aerospace Engineering, 123 MAE-C Bldg., Gainesville, FL 32611, Student Member AIAA.
[4] Graduate Research Assistant, Mechanical and Aerospace Engineering, 123 MAE-C Bldg., Gainesville, FL 32611.
[5] Graduate Research Assistant, Mechanical and Aerospace Engineering, 131 MAE-C Bldg., Gainesville, FL 32611, Student Member AIAA.
[6] Associate Professor, Mechanical and Aerospace Engineering, 336 MAE-B Bldg., Gainesville, FL 32611, Associate Fellow AIAA.

ω_d = damped frequency
ω_n = natural frequency
ζ = damping ratio

I. Introduction

DIELECTRIC barrier discharge (DBD) plasma devices find several applications at atmospheric conditions, such as sterilization (ozone generation, pollutant/toxic waste treatment), electronics (plasma display panels, laser excitation), chemical detection sensors (mass spectroscopy), and flow control (prevent/promote separation, increase lift, reduce drag, aero propulsion). For active flow control applications, DBD devices offer the advantages of lack of moving parts, surface compliance, fast response, low mass and ease of construction, but generally suffer from low flow control authority[1] (fluidic impact).

Typical DBD devices consist of two electrodes placed asymmetrically on either side of a dielectric material. With high-voltage pulsed/AC excitation, the gas locally above the dielectric becomes weakly ionized creating a plasma discharge. This discharge imparts an electrohydrodynamic (EHD) force on the surrounding fluid, inducing a wall jet along the dielectric surface in the direction toward the bottom electrode.

Many efforts have been made to increase the control authority of DBD actuators[2-4], while simultaneously reducing the power requirements. Parameter trends have been studied including input voltage amplitude and frequency, waveform shape (sinusoidal, pulsed, saw tooth, triangular, etc.), material properties, and device geometry. Extensive reviews of plasma actuators for use in flow control[1,5,6] summarize several trends that have been validated repeatedly in experiments. For example, the electrical power consumed by DBD actuators scales exponentially with the sinusoidal input voltage amplitude[7], as $P \propto V^{3.5}$. Furthermore, typical DBD actuators produce a wall jet with velocity of 1-6 m/s occurring 0.5-1 mm above the dielectric surface. Maximum induced velocities have been reported up to ~8 m/s [8] and numerical predictions indicate potential velocities up to ~10 m/s [9]. The net thrust produced ranges from a few mN/m to over 150 mN/m (thrust per unit length electrode), and the power can range up to ~650 W/m depending on both input voltage and frequency and the actuator geometry[2].

The actuator's 'effectiveness'—output per consumed power—is a useful metric for comparing different designs of actuators operated at different voltage levels and frequencies. This power normalization is used to define both 'velocity effectiveness' (velocity per power consumed) and 'thrust effectiveness' (force per power) of DBD plasma actuators. Additionally an indicator of the actuator's mechanical-to-electrical energy conversion efficiency can be computed as the ratio of mechanical output power (force-velocity product) to the electrically consumed input power.

The size and shape of the DBD electrodes play an important role in the device performance. Abe et al.[10] investigated the electrode geometry and found an increase in the momentum transfer to the fluid for thinner copper tape electrodes. The increase is believed to occur from having a stronger local electric field near the edge of a thinner electrode. Hoskinson et al.[11] also demonstrated an increase in momentum transfer while using wire for the powered electrode (instead of rectangular strips). An exponential increase in the induced velocity was shown as the diameter of the high-voltage wire electrode decreased from 0.40 mm to 0.11 mm. Okochi et al.[12] scaled the DBD actuator geometry using semiconductor processing techniques to electrode dimensions as narrow as 1 mm in width and using a 0.5 mm thick dielectric layer, producing velocities up to 3.5 m/s. They concluded that the induced velocity using reduced dimensions demonstrates similar dependency on the applied voltage as larger DBD actuators, and they also confirmed that the maximum induced velocity occurs at the 'tip' of the plasma discharge.

Building on the observations of these prior efforts, in this work we first fabricate DBD devices with microscale dimensions and experimentally analyze their power consumption, induced flow field, and thrust production. Next, the experimental thrust data is applied in a numerical model to simulate the flow response using measured data as the force input, and to compare the numerical prediction with experimental velocity measurements. Various performance metrics for these microscale devices are also compared against the performance of reported macroscale DBD devices.

II. DBD Actuator Fabrication

Devices are constructed using planar batch-fabrication processes, like used in the semiconductor industry. The devices are constructed in a layer-by-layer approach using a variety of selective deposition and etching steps. Photolithographic definition of each layer enables precise control of device geometries and accurate electrode alignment, providing an advantage over the general hand-assembled methods of constructing macroscale DBD actuators. This fabrication approach enables a wide array of materials for the electrodes and dielectric layers and also facilitates the batch-fabrication of many actuators in parallel (currently 57 devices per 100-mm-diameter wafer).

An example devices used in the experiments is shown in Fig. 1a[13]; the leads are offset from the electrode axis such that they do not interfere with the field-of-view for flow visualization and measurement. Figure 1b provides a cross-section schematic of the microscale actuator indicating the device geometry. The electrodes are made of copper and created using sputter deposition. The length of the electrode discharge region is 10 mm long. The exposed (powered) electrode is 1 μm thick and ranges from 10 to 50 μm in width. The encapsulated (grounded) electrode is 0.5 μm thick and ranges in width from 10 μm up to 1 mm. A thin sputtered titanium layer (50 nm) is used underneath each copper layer to promote adhesion of the copper electrodes. All of the devices have a 100 μm gap between the electrodes. The dielectric layer is a polymer material, which is spin-coated and cured. Either a polyimide (PI-2611 from HD Microsystems, ε_r = 3.3, E_d > 2.0x10^6 V/cm) or SU-8 epoxy (SU-8 2025 from MicroChem, ε_r = 3.0, E_d = 1.12x10^6 V/cm) are used in these experiments. The PI-2611 polyimide generally provides thinner layers, while the epoxy-based SU-8 enables thicker films. Hence, the devices using PI-2611 have a 10 μm thick dielectric layer, while the devices with SU-8 have a 20 μm thick dielectric barrier. The fabrication process is illustrated in Fig. 2, showing cross-section diagrams of the process steps. Note that the process steps are shown for the PI-2611 polyimide dielectric; the process steps for using SU-8 are slightly modified (SU-8 is photodefinable and does not require the dry etch and related steps).

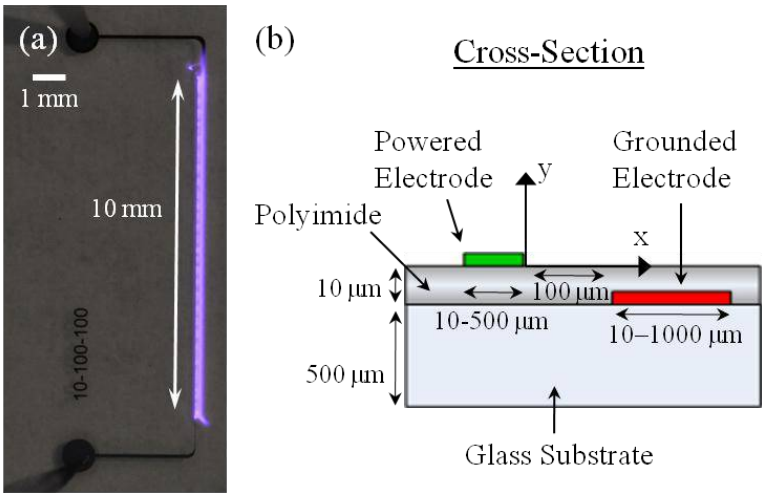

Figure 1. (a) Top view of a single device shown during discharge and (b) cross-section schematic view of the actuator geometry[13]. The nomenclature of the three numbers in part (a) indicates the width (units of μm) of the powered electrode-electrode gap-grounded electrode, respectively. The device shown has a 10 μm wide powered electrode, 100 μm wide electrode gap and 100 μm wide ground electrode, and uses a 10 μm thick polyimide dielectric barrier.

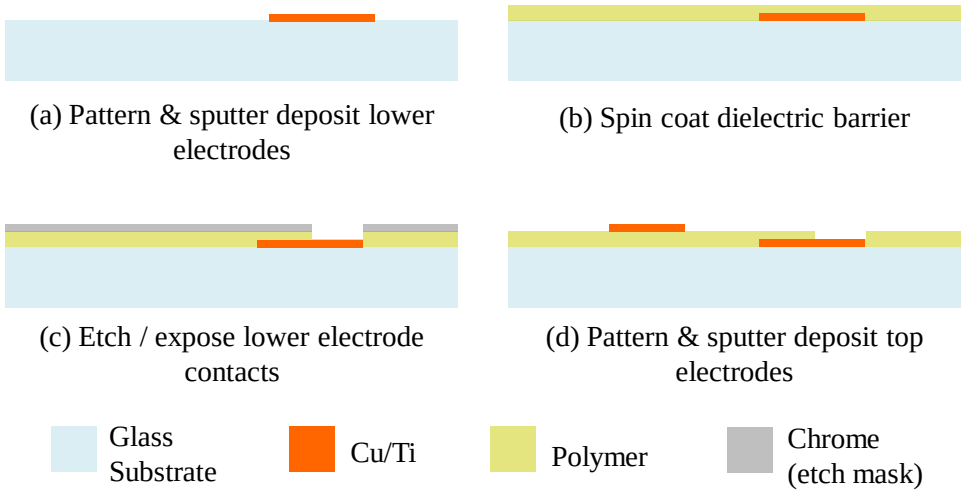

Figure 2. Cross-section diagrams of device fabrication steps (process for PI-2611 polyimide dielectric).

III. Experimental Methods

This section describes the methods used for characterization of the electrical power consumption, the induced velocity flow, and thrust produced by the microscale DBD actuators. The equipment and test setup is presented for the experimental procedures as well as the details of the parameters used for numerical modeling.

A. Electrical Characterization

For testing, a high-voltage sinusoidal input is generated using a function generator (Tektronix AFG3022B) amplified by a high-voltage amplifier (Trek 30/20A). A schematic of the power setup is illustrated in Fig. 3. All of the results are reported for devices operated at 5 kV_{pp} and 1 kHz sinusoidal input. A high-voltage probe (Tektronix P6015A) measures the voltage across the actuator terminals, and a current monitor (Pearson 2100) is used for current measurements at the input to the actuator. A digital oscilloscope (Tektronix DPO3014) captures both of these signals at a sampling rate of 100 MSa/s (million samples per second), providing 10 periods of data with 100,000 sample points per period. The current channel is set to 20 MHz on the oscilloscope, as limited by the bandwidth of the probe. LabVIEW software (National Instruments) is utilized to interface with the oscilloscope and download the voltage and current data. The waveforms are successively downloaded 10 times with a 0.1 second delay between each data set, providing a total 100 periods of data over which the power consumption is averaged. The average power dissipated is computed by integrating the voltage-current product over 100 periods. The time-average power is computed using N data points, as

$$P = \frac{1}{N}\sum_{i=1}^{N} V_i I_i \ \text{(W)}, \tag{1}$$

where V_i and I_i are the instantaneous voltage and current, respectively, corresponding to the i^{th} data point.

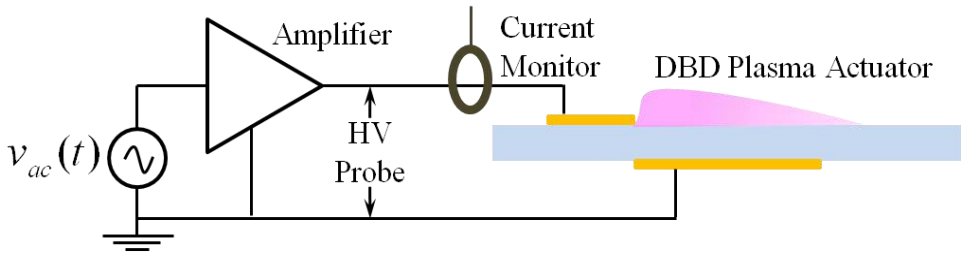

Figure 3. Schematic view of DBD actuator power supply.

B. Mechanical Characterization

Direct thrust measurements are made using a custom-built torsional force balance, which measures the angular deflection of a beam acting against torsion springs. The balance is designed similar to that reported by Castano[14]. The actuator is mounted at the end of a beam moment arm such that the thrust displaces the balance away from an optical displacement sensor. The balance rotates upon a vertical axis defined by an aluminum beam mounted with two torsion springs (one at each end), and an aluminum moment arm deflects horizontally as the axis rotates. The induced thrust from the actuator produces a torque on the balance, which is related to the rotational spring constant (or torsion coefficient) of the torsion springs as well as the angle of deflection about its rotational axis,

$$F = \frac{k_\theta \theta}{l} \ \text{(N)}, \tag{2}$$

where F is the force (N) acting on the balance, l is the length (m) of the moment arm, k_θ is the rotational spring constant (N·m/rad), and θ is the angle of deflection (rads) of the balance arm. The angular displacement is measured using a reflectance-based optical displacement sensor (PhilTec D63). The displacement sensor has 50 nm resolution when operated using a minimum of 256 averages per sample.

The balance is calibrated using logarithmic decrement analysis to extract the rotational spring constant for an underdamped system. This method is based only on the reaction of the balance to an initial displacement (the displacement amount does not need to be known a priori). The rotational spring constant is related to the natural frequency, ω_n, of the balance, according to

$$\omega_n = \sqrt{\frac{k_\theta}{MI}}\ (\text{rad/s}), \tag{3}$$

where *MI* is the mass moment of inertia of the balance (kg·m^2), which is presumed "known." The moment of inertia is computed based on the mass and geometry of each rotating component of the balance. The amplitude and frequency of decaying oscillations from an initial displacement, along with the balance's mass moment of inertia, provide all of the data necessary to extract the spring constant.

The step-by-step extraction analysis is now explained. First, the log decrement, δ, is extracted using the ratio of amplitudes of the decaying oscillations of the balance's response to an initial displacement, according to

$$\delta = \ln\left(\frac{y_n}{y_{n+1}}\right), \tag{4}$$

where y_n and y_{n+1} are the amplitudes of successive oscillation peaks. Using the log decrement, the balance's damping ratio, ζ, is computed (for an underdamped system) as

$$\zeta = \frac{1}{\sqrt{1+\left(\frac{2\pi}{\delta}\right)^2}}. \tag{5}$$

Next, the period of the decaying oscillations is extracted from data, providing the damped frequency, ω_d, of the system. The natural frequency of the balance can now be computed from the damped frequency and damping ratio, according to

$$\omega_n = \frac{\omega_d}{\sqrt{1-\zeta^2}}\ (\text{rad/s}). \tag{6}$$

The rotational spring constant can at last be calculated from Eq. (3). The extracted spring constant using the extraction method described above provides k_θ = 0.0035 N·m/deg which is within the accuracy range of the manufacturer's specified rating for the springs (0.0032 N·m/deg ± 10 %).

C. Fluid Characterization

Particle image velocimetry (PIV) is used to measure the 2D velocity flow-field induced by the plasma discharge. The PIV setup is shown in Fig. 4, and consists of a Nd:YAG laser (New Wave Research) and a LaVision camera (Imager Pro X 4M). The actuator is housed inside a test chamber (2' x 2' x 4' tall) to contain the seed particles and to prevent ambient air currents from affecting the velocity measurement. The ~1 mm thick laser sheet illuminates vaporized Ondina oil (~0.8 µm diameter[15]) as it cuts across the mid-span point of the electrodes. The laser is correctly positioned using alignment markers that were designed on the actuator substrate as part of the fabrication steps. The time interval (*dt*) between image pairs is adjusted for a maximum particle displacement of 5 - 7 pixels. The image pairs are taken at a repetition rate of ~7 Hz.

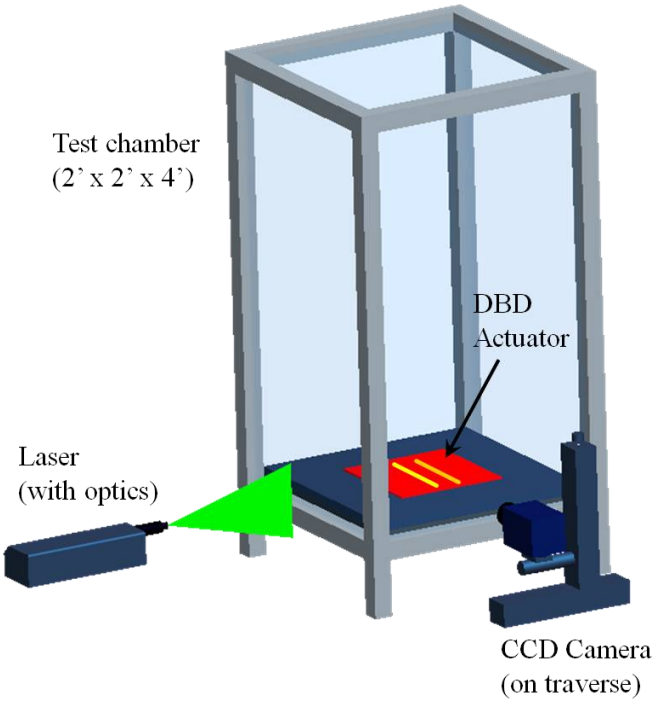

Figure 4. Schematic view of PIV Setup.

Data is processed using LaVision's DaVis 7.2 software. First, the average background image is subtracted from each image to reduce the background noise during the image correlation steps. Then a multi-pass cross-correlation is performed on each image pair by dividing the image into smaller windows with a 50 % overlap. The

correlation is first executed using a window size of 32 x 32 pixels^2, and followed with two successive correlations that are performed using a reduced window size of 16 x 16 pixels^2. An outlier rejection is also performed during the correlation process in order to remove spurious vectors. Finally the velocity field is time-averaged using a total of 300 image pairs, and the resulting vector resolution is 78.6 μm for a 20 mm wide field-of-view.

The convergence of the time-averaged velocity is investigated in Fig. 5 in order to determine whether 300 images provide a statistically sufficient number of image pairs. The data in Fig. 5a displays the x-component of the velocity measured at x = 3 mm and y = 0.5 mm, and in Fig. 5b for x = 8 mm and y = 1.5 mm. The velocity remains fairly constant at 3.0 and 3.5 kV_{pp} with fluctuations (standard deviation / average velocity) within 2.1 % of the mean velocity. At 4 kV_{pp}, the data at x = 3mm varies slightly more, within 2.4 % of the mean velocity value, although at x= 8 mm (Fig. 5b) the velocity variation is only 1.3 %. The overall variation in the averaged velocity is within 3.0 % and permits confidence in our time-averaged velocity measurements.

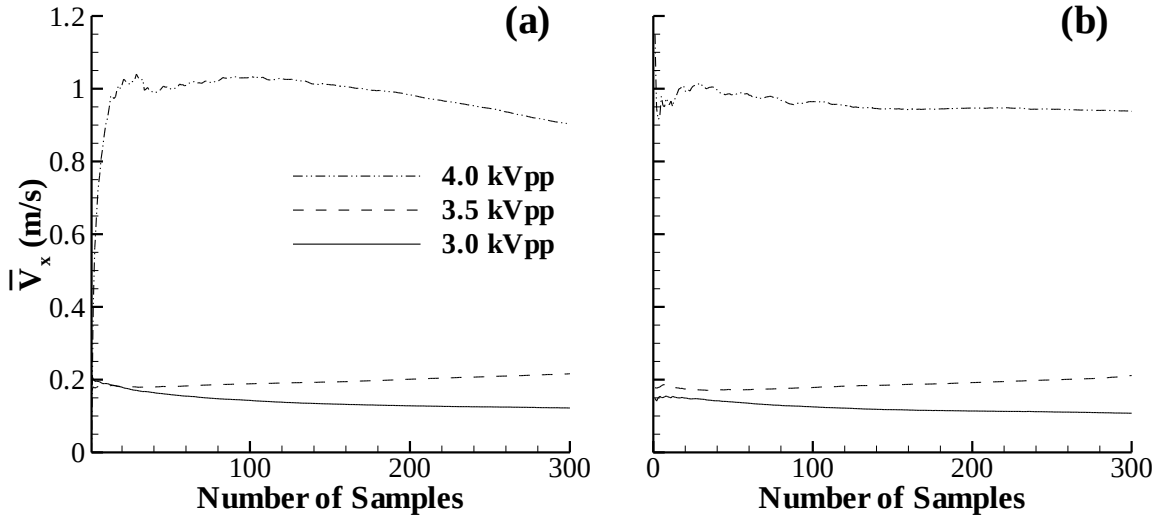

Figure 5. Velocity convergence plots over 300 image pairs for the x-component of velocity at (a) x = 3.0 mm, y = 0.5 mm, and (b) x = 8.0 mm, y = 1.5 mm.

D. Numerical Model

Using the force obtained from the thrust stand experiment as an input to a fluid dynamics simulation, the actuator flow fields are predicted and later compared with the PIV results. The thrust data is applied as a body force in a Navier-Stokes flow simulation. Since the thrust data simply gives a scalar quantity for the net body force, the body force is distributed spatially using the physics-based reduced order model by Singh and Roy[16]. The force in the horizontal direction is given as

$$F_x = F_{x0}\phi_0^4 \exp\left[-\left(\frac{y - y_0}{x} \right)^2 - \beta_x \left| x - x_0 \right|^2 \right] (\mathrm{N/m^3}), \tag{8}$$

and the vertical force is neglected. The vertical force is much smaller than the horizontal force, and only the horizontal force is measured by the thrust stand. The net integrated body force predicted by the model is scaled to match the net force obtained from the thrust stand experiment, shown in Fig. 8 (in Results section).

$$F_{net} = \iint_A F_x \, dA \, (\mathrm{N/m}), \tag{9}$$

Eq. (9) is satisfied by scaling the constant F_{x0} for the body force distribution given in Eq. (8). Figure 6 displays a sample plot of the body force distribution, the lower-right edge of the exposed electrode is positioned at (x, y) = (0,0).

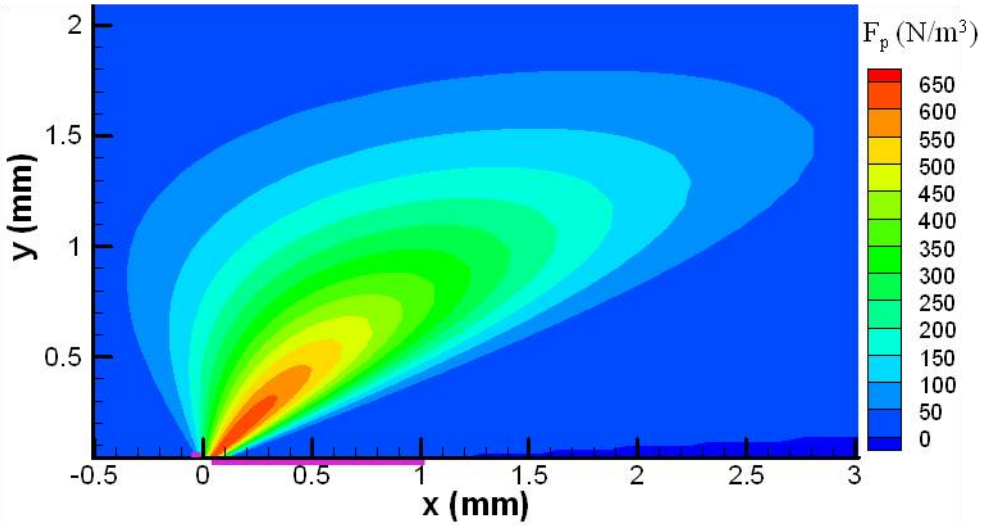

Figure 6. Body force distribution[16] for the device with 10-100-1000 µm geometry, 4kV$_{pp}$ case. The electrode geometry is indicated at the bottom of the figure for reference.

The resulting spatial distribution for the body force is input into the commercial flow modeling software FLUENT™. The domain size for the simulation is 35 mm x 15 mm, with 8784 finite volume cells. The grid is locally refined near the plasma actuator to properly resolve the plasma actuator body force. A standard pressure-based solver is used with a second-order upwind spatial discretization. The body force is programmed using a user-defined function as a source term in the momentum equation. The bottom boundary is taken to be the dielectric surface, and a solid wall boundary is used. The pressure inlet boundary condition is used for the left boundary, and pressure outlet boundary conditions are used for the top and right boundaries. Convergence is declared when the residuals of all the variables fall below 10^{-3}.

IV. Results

The following section presents the results from the microscale DBD actuator experiments. Power, thrust and velocity data are presented and followed with simulation results from the numerical models. Comparisons are then made between the experimental PIV data and numerical predictions.

A. Power Measurements

Figure 7 shows the power consumed for microscale DBD devices having varying electrode widths operated at 1 kHz[13]. These data are measured from devices having a 10 µm thick dielectric layer (PI-2611). The power consumption shows little dependency on the exposed electrode width. However, slight differences are observed for the grounded electrode width; a wider ground electrode slightly increases the power dissipation. The ability to store charge (and thus dissipate power) is dependent upon the effective plasma resistance, which is related to the discharge cross-sectional area as well as the surface charge on the dielectric and the distribution of electric conduction paths within the plasma. Using a narrow ground electrode can limit the effective plasma resistance and power consumption, reducing the actuator's performance. This was shown by Enloe et al.[17], where the maximum induced velocity is limited by the area of the grounded electrode, but no longer increases above some saturation voltage (dependent on device geometry). The dependency of power on the applied voltage is best captured using a logarithmic scale; the slope of the fit line (3.5) indicates that microscale DBD actuators follow a similar exponential relationship to the macroscale actuators. The average power consumed (per unit length of electrode) reaches 15 W/m at 5 kV$_{pp}$ and 1 kHz.

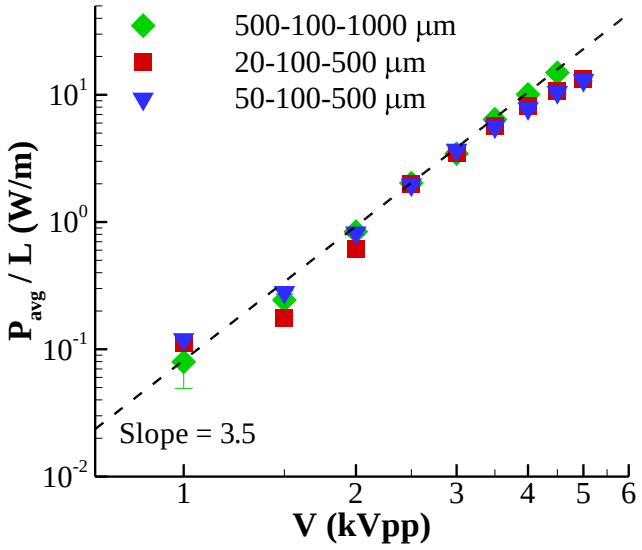

Figure 7. Power consumed for microscale DBD devices with varying electrode geometries plotted against applied voltage, operated at 1 kHz[13].

B. Thrust Measurements

Thrust data is presented in Fig. 8 for four different cases based on two actuator geometries (100 μm & 1000 μm wide ground electrodes) and two dielectric materials (PI-2611 and SU-8 2025). The devices with 1000 μm wide ground electrodes show consistently larger forces compared with the smaller (100 μm) ground electrodes. For both geometries, the actuators using PI-2611 polyimide produces larger thrust values. This can be attributed to the thickness of the two dielectrics: the SU-8 has twice as thick of a dielectric layer (20 μm) compared with the PI-2611 (10 μm). For a given voltage, the electric field is stronger across the thinner dielectric, providing larger thrust measurements. The exponential relationship between the force and voltage is indicated by the slope of the data in Fig. 8. In increasing order, the slopes of the four data trends are equal to 2.2, 3.4, 3.6, and 6.6. Maximum thrust produced for devices with PI-2611 reaches 3 mN/m at 5 kV_{pp}, while the max thrust for devices using SU-8 dielectric reaches 2.2 mN/m at 6 kV_{pp}.

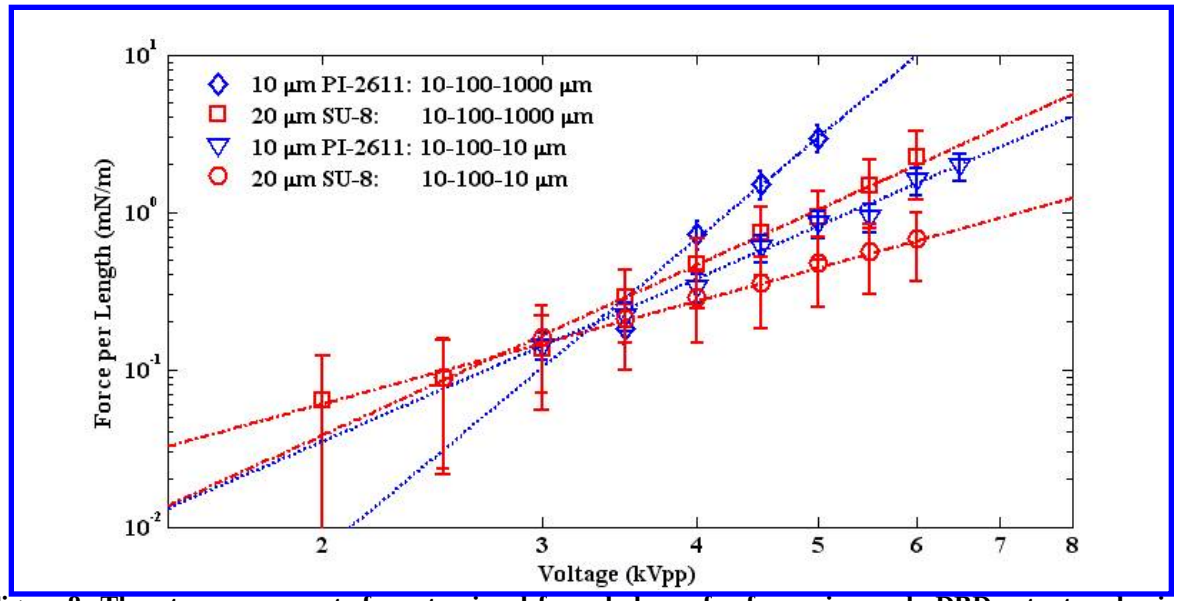

Figure 8. Thrust measurements from torsional force balance for four microscale DBD actuators having two geometries (100 μm & 1000 μm wide ground electrodes) and two dielectric materials (PI-2611 and SU-8 2025).

C. Velocity Measurements

PIV data is shown in Figs. 9 and 10 for two devices having different ground electrode widths. Figure 9 displays velocity data for a device with 10-100-1000 µm geometry (10 µm wide powered electrode, 100 µm electrode separation, and a 1000 µm wide ground electrode) and utilizing a 10 µm thick polyimide dielectric barrier. Velocity fields are shown for 3, 4 and 5 kV_{pp} input voltages. With increasing voltage, the thickness of the wall jet decreases as the near-wall flow grows stronger. The downstream fluid effect also increases with input voltage. At 3, 4 and 5 kV_{pp} the maximum induced velocities reach 0.21, 1.02 and 1.93 m/s, respectively. At 5 kV_{pp} the microscale actuator demonstrates a wall jet with comparable velocity and profile to macroscale DBD actuators. However at reduced voltages the fluidic impact is much more local to the device, as observed in the 3 kV_{pp} velocity data where the range of the wall jet maximum velocities reach only 3 mm downstream.

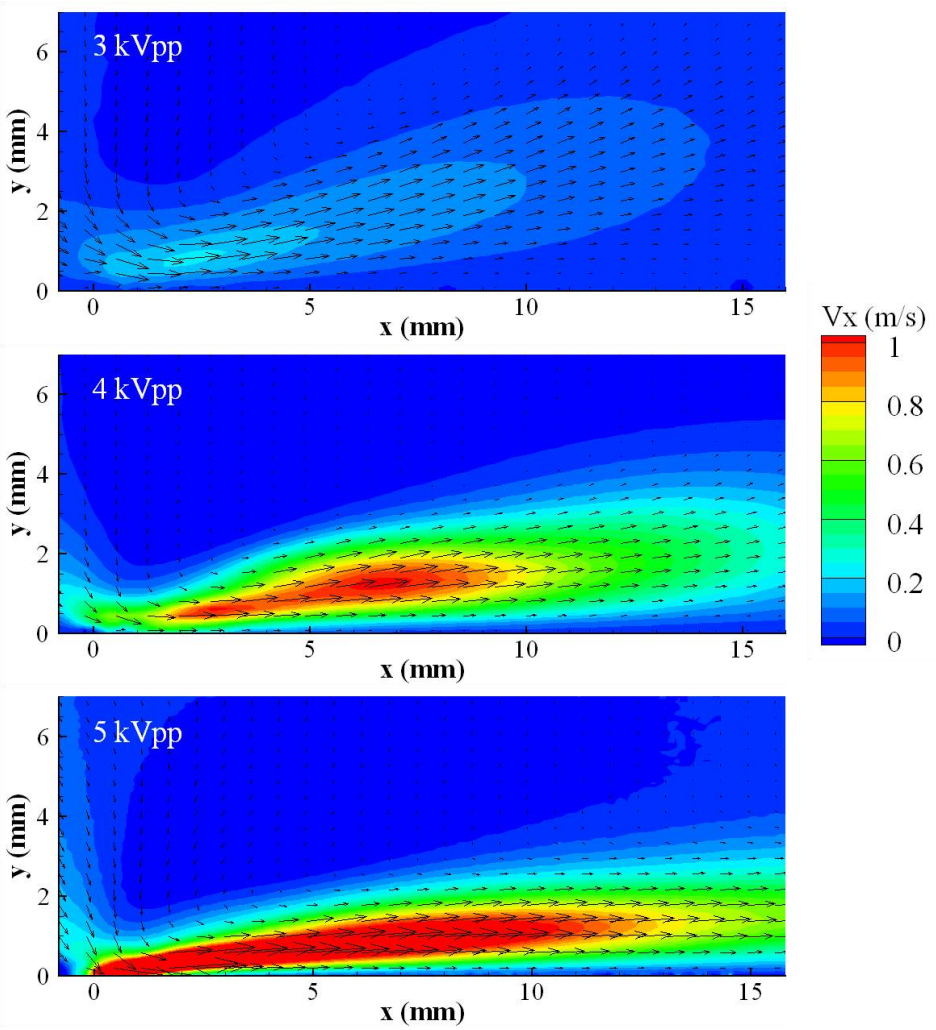

Figure 9. PIV data for a microscale DBD actuator with 10-100-1000 µm geometry operated at 3 kV_{pp} (top), 4 kV_{pp} (middle), and 5 kV_{pp} (bottom). The device has a 10 µm thick polyimide dielectric layer.

Figure 10 presents velocity data for a device with 10-100-100 µm geometry and also having a 10 µm thick polyimide dielectric barrier. The ground in this case is an order of magnitude smaller in width than in the previous case. The affect of the reduced ground electrode size is observed in the data as the velocities are significantly reduced: at 3 and 4 kV_{pp}, the maximum velocities achieved reach just 0.09 and 0.39 m/s, respectively. These velocities are less than half that produced from the actuator data with the 10x larger ground electrode. At 3 kV_{pp} the range of the wall jet extends only ~3 mm downstream; it decays below 0.05 m/s at 5 mm downstream. On one hand, the limited extent of the wall jet could be considered a weakness. Conversely, the spatial compactness could be leveraged to create distributed arrays of actuators with high spatial resolution.

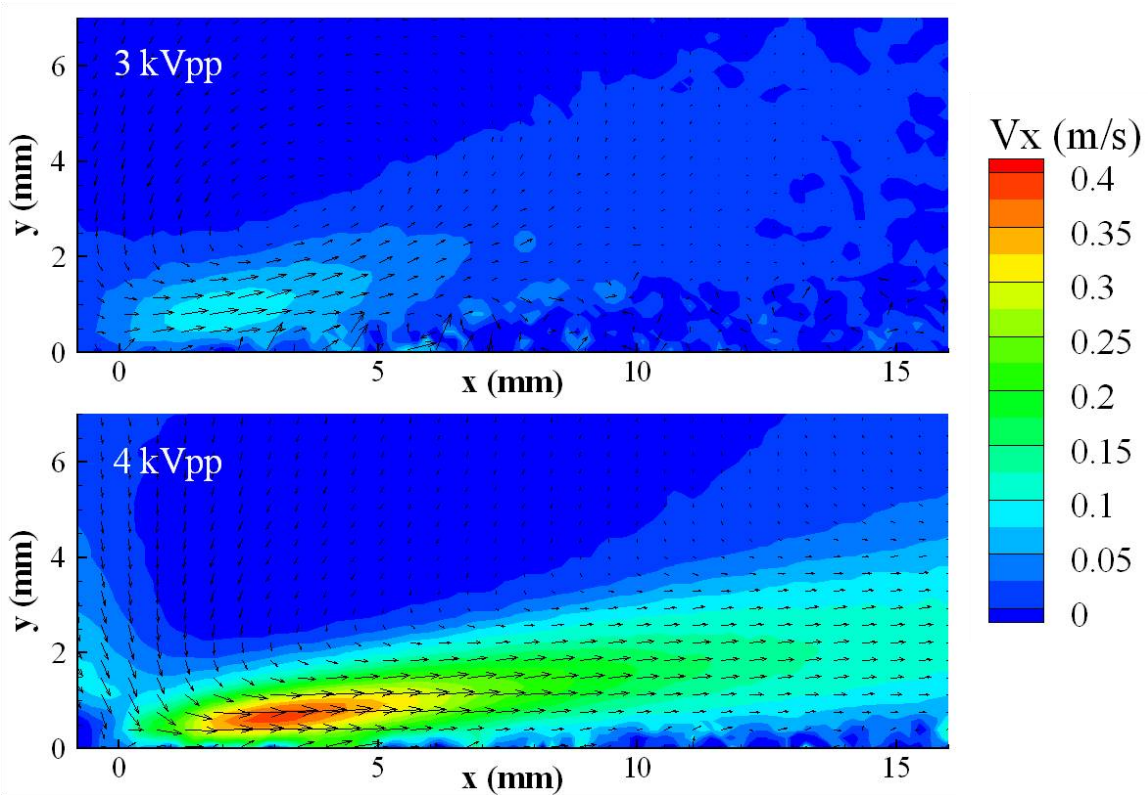

Figure 10. PIV data for microscale DBD actuator with 10-100-100 µm geometry operated at 3 kV_{pp} (top) and 4 kV_{pp} (bottom). The device has a 10 µm thick polyimide dielectric layer.

If the ground electrode is too narrow, it can limit the extent of the discharge, in turn limiting the actuator performance. This is best illustrated visually as shown in Fig. 11. A device with a 100 µm wide ground electrode is shown in Fig. 11a, and a device with a 1 mm wide ground in Fig. 11b. As the voltage increases from 3 kV_{pp} to 4 kV_{pp}, the device with the narrower ground electrode (Fig. 11a) is limited in the extent of discharge while the device with the larger ground electrode continues to increase in discharge area. This affect can be observed in the actuator's performance data: the thrust is consistently larger for the devices with a wider ground electrode, and the induced velocity has stronger downstream affect as well.

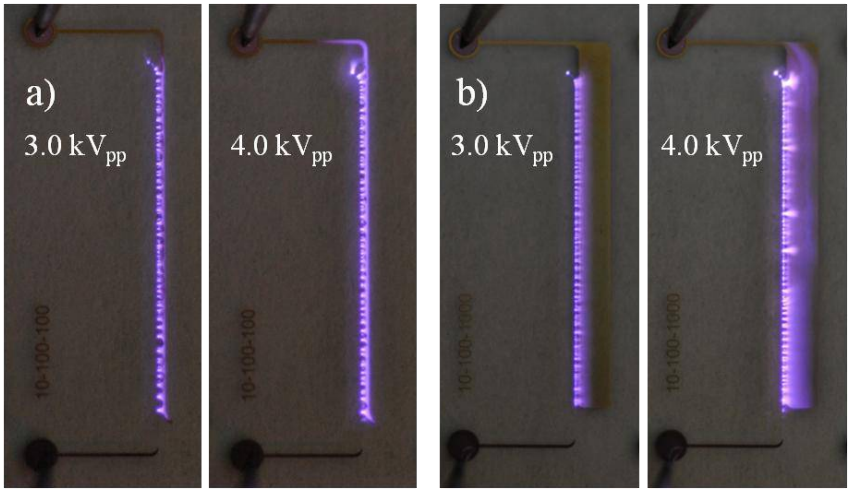

Figure 11. Discharge shown for two devices using 3 kV_{pp} and 4 kV_{pp} applied voltages. With increasing voltage, the extent of the discharge is limited for the actuator with 100 µm wide ground (a), while the discharge length continues to increase for the device with 1mm wide ground electrode (b).

D. Numerical Simulations

Comparisons between the numerical and PIV results are shown in Figs. 12 and 13. These figures correspond to grounded electrode widths of 1000 µm and 100 µm, respectively. In both cases, the applied voltage was 4 kV_{pp}. Figure 12 indicates a good match for the peak velocity near the actuator, but the numerical results do not predict the sharp drop-off in the maximum velocity that occurs ~10 mm downstream of the actuator. In Fig. 13, this drop-off is even more drastic and causes an even earlier divergence from the numerical results. At 5 mm downstream, the velocity profiles for the 100 µm case do not show as close a match compared with those for the 1000 µm case.

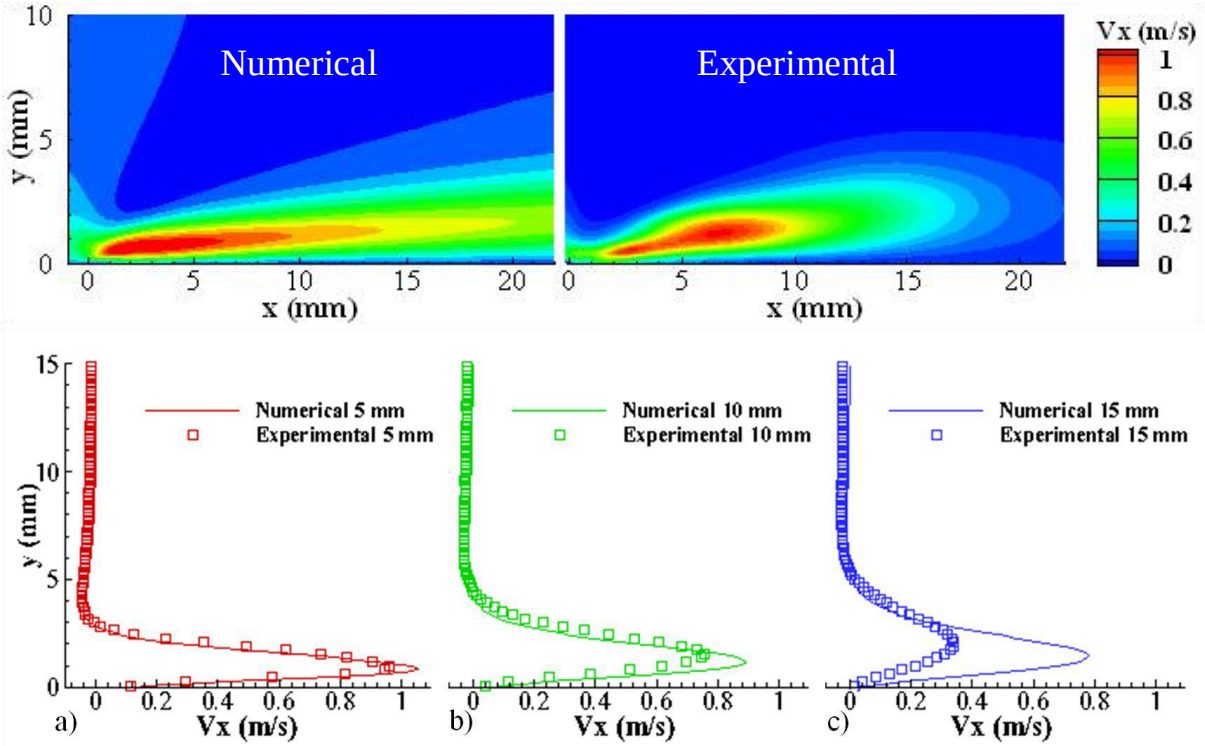

Figure 12. Comparison between numerical data (top left) and PIV data (top right) for the 10-100-1000 µm geometry, 4kV_{pp} case. Velocity profiles for Vx are shown for 5 mm (a), 10 mm (b) and 15 mm (c) downstream of the actuator.

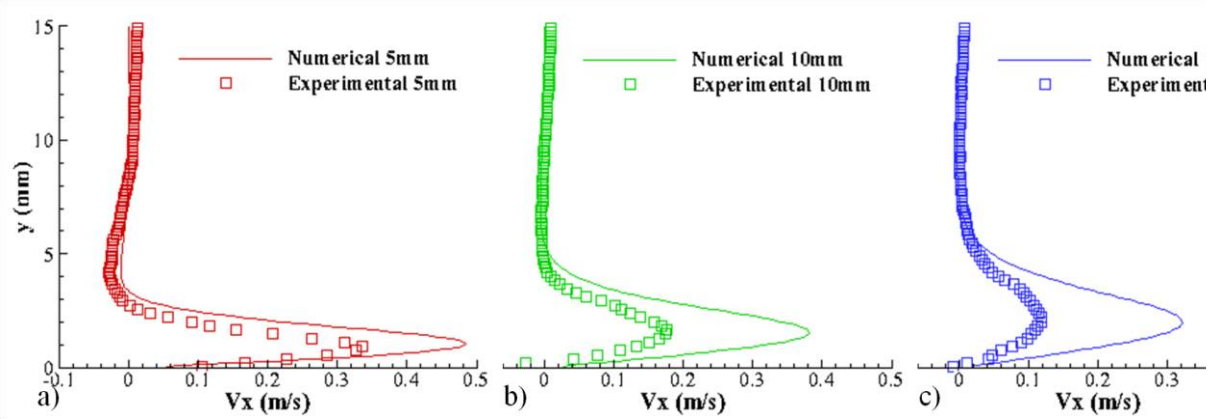

Figure 13. Comparison between numerical and PIV data for the 10-100-100 µm geometry, 4 kV_{pp} case. Velocity profiles for Vx are shown for 5 mm (a), 10 mm (b) and 15 mm (c) downstream of the actuator.

Overall, the results show a good match for the thickness of the wall jet but do not predict the correct downstream decay of the wall jet. The numerical model is the most accurate in the region near the actuator, but the decay in the strength of the wall jet is much more drastic in the experimental case. This could be attributed to the fact that the

reduced-order model was developed for a macro-DBD geometry. As the size of the actuator is increased, the numerical results show a better match with the PIV results, because the wall jet does not lose strength as rapidly. The reduced-order numerical model accurately matches with the larger device data which exemplifies macroscale actuator performance. The discrepancy between simulated and measured data for the microscale geometry device indicates that the model should be modified to appropriately predict the downstream decay in velocity, possibly by taking into account the electrode geometry. Furthermore, any experimental errors in the measurement of the net thrust will propagate into the numerical simulation, which is sensitive to the accuracy of the plasma body force in order to yield a good prediction.

V. DBD Actuator Comparison: Micro vs. Macro

The data collected in these experiments is compared with several reported macroscale actuators found in recent literature[2,8,10] and summarized in Table 1[13]. The actuator volume and mass are computed using the reported geometries provided in each reference, with the electrode lengths normalized to 1 meter. The first row in the table reports the actuator thrust effectiveness (force produced per consumed power). One of the reported actutaors[10] indicates similar thrust and power values to the microscale actuator, while the other macroscale device[2] indicates significantly larger thrust production and power consumption. However, all three actuators demonstrate equivalent thrust effectiveness. Similarly, the fourth row in the table reports the velocity effectiveness. The microscale actuator shows a 63% increase compared with Ref. 8, and an 86% increase compared with Ref. 10. The final row in Table I reports the actuator energy conversion efficiency, η, for the cases in which both velocity and force data are reported. The efficiency is computed as the ratio of mechanical power (output) to electrically consumed power (input), according to

$$\eta = \frac{F v_{\max}}{P} . \tag{7}$$

The microscale DBD provides a 31% increase in energy conversion efficiency compared with Ref. 10. On a per-volume or per-mass basis, the microscale actuator outperforms the macroscale actuators in both force and velocity metrics. This is due the significant size reduction of the microscale DBD actuators. In addition, employment of thin-film dielectric materials and scaled device geometry reduces the breakdown voltage required for discharge.

VI. Conclusion

In conclusion, we have demonstrated the fabrication, flow inducement and thrust production of DBD devices having microscale electrode dimensions. Devices that were operated at 5 kV_{pp} and 1 kHz consumed ~15 W/m on average. The power dissipated was shown to have stronger dependency on the grounded electrode width and weak dependence on the exposed electrode width. The power consumption for microscale DBD actuators scales with $V^{3.5}$ indicating that the microscale devices follow similar power trends to macroscale DBD actuators[7]. The reduction in power consumption is attained from the reduced breakdown voltage gained from using a thin dielectric layer.

Thrust measurements indicate body forces up to 3 mN/m for devices having a 10 μm thick dielectric barrier and operated at 5 kV_{pp}. Devices with a wider ground electrode produced larger thrust values than devices with narrower ground electrodes. Two dielectric materials were used to achieve different thicknesses, having similar permittivity values. The devices with the thinner dielectric layer (10 μm thick PI-2611) provided more thrust than those with thicker dielectric (20 μm thick SU-8) due to the increased electric field strength at a given voltage across the thinner dielectric barrier.

PIV data show significant dependence on both input voltage as well as the ground electrode size. With increasing voltage the thickness of the wall jet is reduced, and the induced velocity increases and produces a stronger downstream fluidic impact. At 5 kV_{pp} the velocity reaches ~2 m/s for a device having a 1 mm wide ground electrode and a 10 μm thick polyimide dielectric, indicating comparable velocity magnitude and profile to standard macroscale DBD actuators. When the ground electrode width was reduced by an order of magnitude (from 1 mm to 100 μm), the maximum induced velocity at a given voltage decreased below half of that induced from the larger ground electrode. However, the reduced size, low-voltage (3 kV_{pp}) devices produce localized disturbances to the flow-field with lower power consumption than their macroscale counterparts. Arrays of such microscale DBD actuators could enable distributed flow control systems. For example, one could envision large arrays where individual "pixels" could be addressed/actuated individually for precise locations of fluidic control.

Numerical simulations were implemented based on experimental data from microscale DBD thrust measurements. The simulation results predict good agreement with the thickness of the induced wall jet, although do not predict well the exponential decay of the velocity downstream from the actuator. Comparison of the velocity

Table 1. Micro- and Macro-DBD actuator performance metrics: comparing actuator thrust and velocity to power consumption, device geometry and material properties[13].

Performance Metrics	**Micro-DBD** V_{max} = **2m/s** Force = 3 mN/m P_{avg} = 15 W/m (5kV_{pp}, **1kHz**)	**Macro-DBD[2]** V_{max} = N/A Force = 120 mN/m P_{avg} = 590 W/m (74kV_{pp}, **1kHz**)	**Macro-DBD[8]** V_{max} = **2m/s** Force = N/A P_{avg} = 25 W/m (24kV_{pp}, **1kHz**)	**Macro-DBD[10]** V_{max} = 1.4 m/s Force = 3.9 mN/m P_{avg} = 20 W/m (20kV_{pp}, **1kHz**)
Thrust 'Effectiveness' [Force per Normalized Power] (mN/W)	0.20	0.20	---	0.20
Thrust Density [Force per Actuator Volume] (mN/ m^3)	5.29×10^6	2.57×10^5	---	6.84×10^4
Thrust per Actuator Mass	0.215	9.70×10^{-3}	---	4.10×10^{-3}
Velocity 'Effectiveness' [Velocity per Normalized Power] (m/s) / (W/m)	0.13	---	0.08	0.07
Velocity per Actuator Volume (m/s) / m^3	3.53×10^6	---	9.52×10^4	2.46×10^4
Velocity per Actuator Mass (m/s) / g	1.41	---	7.60×10^{-2}	1.44×10^{-2}
Actuator Efficiency	4.00×10^{-4}	---	---	2.73×10^{-4}

profiles with PIV data at three downstream locations showed better agreement for the larger geometry (1 mm wide ground electrode), suggesting that the model may be better suited for macroscale DBD actuators (for which it was developed). A modified model is needed to correctly predict the decay in velocity for microscale geometries.

The microscale DBD actuator performance was summarized and compared with reported macroscale data. The actuator 'effectiveness' was used to compare thrust and velocity with power consumption; the microscale actuators demonstrate equivalent thrust effectiveness with macroscale devices indicating that the DBD actuator thrust performance scales linearly with size reduction. The velocity effectiveness of microscale actuators showed 63% and 86% improvement compared with two macroscale devices. In the case where force and velocity data were both reported, the microscale actuator demonstrated 31% higher energy conversion efficiency compared with the macroscale actuator. Overall, the microscale DBD actuator induced velocity, thrust, and power consumption scale favorably with size reduction. The compact size and low mass of the micro actuators make them implementable with minimal weight penalty.

Acknowledgments

This work was supported in part by AFOSR Grant monitored by Dr. Douglas Smith and ARO Grant # W911NF-09-1-0511. The authors also gratefully acknowledge the assistance from the staff of the UF Nanoscale Research Facility.

References

[1]Cattafesta, L. N., and Sheplak, M., "Actuators for Active Flow Control," *Annual Review of Fluid Mechanics*, Vol. 43, 2011, pp. 247-272.

[2]Thomas, F. O., Corke, T. C., Iqbal, M., Kozlov, A., and Schatzman, D., "Optimization of Dielectric Barrier Discharge Plasma Actuators for Active Aerodynamic Flow Control," *AIAA Journal*, Vol. 47, No. 9, 2009, pp. 2169-2178.

[3]Corke, T. C., Post, M. L., and Orlov, D. M., "SDBD Plasma Enhanced Aerodynamics: Concepts, Optimization and Applications," *Progress in Aerospace Sci.*, Vol. 43, 2007, pp. 193-217.

[4]Roth, J. R., and Dai, X., "Optimization of the Aerodynamic Plasma Actuator as an Electrohydrodynamic (EHD) Electrical Device," *44th AIAA Aerospace Sciences Meeting and Exhibit*, Reno, NV, Jan. 9-12, 2006, AIAA-2006-1203.

[5]Moreau, E., "Airflow Control by Non-Thermal Plasma Actuators," *J. Phys. D: Appl. Phys.*, Vol. 40, 2007, pp. 605-636.

[6]Corke, T. C., Enloe, C. L., and Wilkinson, S. P., "Dielectric Barrier Discharge Plasma Actuators for Flow Control," *Annual Review of Fluid Mechanics*, Vol. 42, 2010, pp. 505-529.

[7]Enloe, C. L., McLauchlin, T. E., VanDyken, R. D., Kachner, K. D., Jumper, E. J., and Corke, T. C., "Mechanisms and Responses of a Single Dielectric Barrier Plasma Actuator: Plasma Morphology," *AIAA Journal*, Vol. 42, No. 3, 2004, pp. 589-594.

[8]Forte, M., Jolibois, J., Pons, J., Moreau, E., Touchard, G., and Cazalens, M., "Optimization of a Dielectric Barrier Discharge Actuator by Stationary and Non-Stationary Measurements of the Induced Flow Velocity: Application to Airflow Control," *J. Exp. Fluids*, Vol. 43, 2007, pp. 917-928.

[9]Likhanskii, A. V., Shneider, M. N., Opaits, D. F., Miles, R. B., and Macheret, S. O., "Limitations of the DBD Effects on the External Flow," *48th AIAA Aerospace Sciences Meeting*, Orlando, FL, Jan. 4-7, 2010, AIAA-2010-470.

[10]Abe, T., Takizawa, Y., Sato, S., and Kimura, N., "Experimental Study for Momentum Transfer in a Dielectric Barrier Discharge Plasma Actuator," *AIAA Journal*, Vol. 46, No. 9, 2008, pp. 2248-2256.

[11]Hoskinson, A. R., Hershkowitz, N., and Ashpis, D. E., "Force Measurements of Single and Double Barrier DBD Plasma Actuators in Quiescent Air," *J. Phys. D: Appl. Phys.*, Vol. 41, No. 24, 2008, 245029.

[12]Ocochi, S., Kasagi, N., Suzuki, Y., and Ito, S., "Development of Micro Plasma Actuator for Active Flow Control", *Exp. Heat Transfer, Fluid Mechanics and Thermodynamics, 7th World Conf. on*, Krakow, Poland (2009).

[13]Zito, J. C., Durscher, R. J., Soni, J., Roy, S., and Arnold, D. P., "Flow and Force Inducement using Micron Size Dielectric Barrier Discharge Actuators," *Appl. Phys. Lett.*, Vol. 100, 2012, 193502.

[14]Gamero-Castano, M., "A Torsional Balance for the Characterization of MicroNewton Thrusters", *Rev. Sci. Inst.*, Vol. 74, 10 (2003).

[15]Model 9302 Atomizer, Instruction Manual, TSI, September, 2000.

[16]Singh, K. P., and Roy, S., "Force Approximation for a Plasma Actuator Operating in Atmospheric Air," *J. Appl. Phys.*, Vol. 103, 2008, 013305.

[17]Enloe, C. L., McLauchlin, T. E., VanDyken, R. D., Kachner, K. D., Jumper, E. J., Corke, T. C., Post, M., and Haddad, O., "Mechanisms and Responses of a Single Dielectric Barrier Plasma Actuator: Geometric Effects," *AIAA Journal*, Vol. 42, No. 3, 2004, pp. 595-604.